

# SFO: Learning PDE Operators via Spectral Filtering

Noam Koren <sup>\*1</sup> Rafael Moschopoulos <sup>\*2</sup> Kira Radinsky <sup>\*1</sup> Elad Hazan <sup>\*2</sup>

## Abstract

Partial differential equations (PDEs) govern complex systems, yet neural operators often struggle to efficiently capture the long-range, nonlocal interactions inherent in their solution maps. We introduce Spectral Filtering Operator (SFO), a neural operator that parameterizes integral kernels using the Universal Spectral Basis (USB)—a fixed, global orthonormal basis derived from the eigenmodes of the Hilbert matrix in spectral filtering theory. Motivated by our theoretical finding that the discrete Green’s functions of shift-invariant PDE discretizations exhibit spatial Linear Dynamical System (LDS) structure, we prove that these kernels admit compact approximations in the USB. By learning only the spectral coefficients of rapidly decaying eigenvalues, SFO achieves a highly efficient representation. Across six benchmarks—including reaction-diffusion, fluid dynamics, and 3D electromagnetics—SFO achieves state-of-the-art accuracy, reducing error by up to 40% relative to strong baselines while using substantially fewer parameters.

## 1. Introduction

Many phenomena in physics, engineering, and the natural sciences are governed by partial differential equations (PDEs). Classical numerical solvers (e.g., finite elements, finite differences, and finite volumes (Reddy, 1993; Morton & Mayers, 2005; Eymard et al., 2000)) are often expensive at high resolution, where very fine discretizations are needed (Tang & Lin, 2017). This has motivated neural operators: learned models that approximate the PDE solution operator, i.e., a mapping from an input function (e.g., boundary conditions) to the corresponding solution field. Once trained, a neural operator can amortize simulation cost across many queries, enabling fast inference for new PDE instances. Fur-

<sup>1</sup>Department of Computer Science, Technion - Israel Institute of Technology, Haifa, Israel <sup>2</sup>Department of Computer Science, Princeton University, Princeton, New Jersey, USA. Correspondence to: Noam Koren <noam.koren@campus.technion.ac.il>.

thermore, unlike traditional approaches that require explicit knowledge of the governing equations, neural operators are data-driven and can learn the solution map directly from observations without knowing the underlying PDE.

A central challenge in neural operator design is representing nonlocal interactions efficiently (e.g., FNO (Li et al., 2021), MPNN (Brandstetter et al., 2022)). Many PDE solution operators exhibit long-range dependencies, where the solution at a point depends on distant regions of the domain (e.g., elliptic PDEs, nonlocal fractional diffusion, etc. (Herman)). Capturing such behavior is difficult, as it requires transmitting information across the entire domain while maintaining a compact and efficient model.

In this work, we take a dynamical systems perspective on PDE solution operators and introduce **SPECTRAL FILTERING OPERATOR (SFO)**, a neural operator that parameterizes the integral kernel using the Universal Spectral Basis (USB). Originally proposed for learning Linear Dynamical Systems (LDS) (Hazan et al., 2017), the USB consists of the eigenvectors of the Hilbert matrix. Unlike Fourier bases (which bias towards smooth, periodic functions) or learned bases (which risk overfitting), the USB is fixed, globally supported, and exhibits a rapidly decaying spectrum.

SFO adapts the Spectral Transform Unit (STU) from sequence modeling (Agarwal et al., 2023) to the spatial operator setting. Rather than learning a kernel point-by-point, we represent the global kernel as a truncated expansion in the leading USB modes and learn only the spectral mixing coefficients. This strategy is theoretically justified by the structural properties of PDE solution operators: we analyze a representative setting where the discrete Green’s kernel exhibits spatial LDS structure. Because the USB provides exponential spectral decay for such systems, the operator’s energy concentrates in the leading modes, enabling SFO to efficiently capture long-range, marginally stable dynamics with a highly compact representation.

Across six PDE benchmarks, SFO achieves consistent state-of-the-art accuracy, with up to 40% error reduction while using significantly fewer parameters than prior work.

The contributions of this work are:

1. We introduce a fixed, data-independent global spectral parameterization for neural-operator kernels based on the

Universal Spectral Basis (USB), enabling compact representations of long-range interactions.

2. We design SFO, a neural operator that realizes this parameterization via STU-style spectral filtering and efficient FFT-based integral evaluation.
3. For linear, shift-invariant 1D three-point stencil PDE discretizations, we prove LDS structure in space of the discrete integral kernel and derive a USB truncation error bound showing that  $\epsilon$ -accuracy is achievable with  $\tilde{\mathcal{O}}(\log(1/\epsilon))$  USB modes.
4. We demonstrate consistent state-of-the-art performance over six PDE benchmarks, achieving up to 40% error reduction with significantly fewer parameters than prior work.

An anonymized code repository is available.<sup>1</sup>

## 2. Related Work

Neural operator architectures differ primarily in how they represent and parameterize the solution operator. We categorize existing approaches into five major classes: DeepONet-based, Fourier-based, Graph-based, Physics-Informed, and Explicit Kernel Representation. Our comparative analysis includes a broad set of baselines from each class, covering the established architectures in the PDENNEval survey (Wei et al., 2024) (DeepONet, FNO, UNO, MPNN, PINO, UNet) as well as the recent kernel-learning method SVD-NO.

**DeepONet-Based.** DeepONet (Lu et al., 2021) and its variants (F-DeepONet (Zhu et al., 2023), PI-DeepONet (Lin et al., 2023)) use a branch–trunk decomposition to map input fields and coordinates into a latent space. These coordinate-based models can be costly at high resolution. Related attention-based operator models (e.g., Galerkin Transformers (Cao, 2022)) capture global interactions but often incur higher compute and memory costs and scale less favorably with grid size; we include DeepONet as a baseline.

**Fourier-Based.** FNO (Li et al., 2021) and its variants (e.g., WNO (Tripura & Chakraborty, 2023), SFNO (Bonev et al., 2023), Geo-FNO (Li et al., 2023a), DPNO (Ma et al., 2024), CNO (Raonic et al., 2023), LNO (Cao et al., 2023), KNO (Xiong et al., 2023), UNO (Rahman et al., 2023)) learn multipliers on a truncated set of Fourier modes, biasing them toward low frequencies. If the true kernel exhibits strong off-diagonal decay, capturing it well may require many modes, making low-frequency truncation an inefficient inductive bias. We include FNO and UNO as baselines.

**Graph-Based.** For unstructured domains, GNN-based models (e.g., GNO (Li et al., 2020), GINO (Li et al., 2023b), MPNN (Brandstetter et al., 2022)) approximate the operator via message passing on graph edges. They handle irregular

geometries but can struggle with long-range interactions and oversmoothing; we use MPNN as a baseline.

**Physics-Informed.** Methods such as PINO (Li et al., 2024) incorporate PDE structure directly into the loss, enabling learning guided by physical laws. This approach is orthogonal to architecture choice; we include PINO as a baseline.

**Explicit Kernel Representation.** These methods learn the kernel explicitly. SVD-NO (Koren et al., 2025) uses a low-rank decomposition with learned basis functions, which can be expressive but sensitive to data coverage and overfitting; we include SVD-NO as a comparison.

Additionally, UNet is included as a generic neural surrogate baseline, consistent with common practice in the field.

A parallel line of research introduced the **Universal Spectral Basis (USB)**, derived from the eigenvectors of the Hilbert matrix, motivated by learning long-range dependencies in LDS (Hazan et al., 2017). The USB provides a fixed orthonormal set of globally supported modes with rapid spectral decay, offering an attractive basis for compact spectral representations. Unlike Fourier bases, USB modes are not frequency-ordered and exhibit rapid decay for a broad class of LDS, while remaining fixed and data-independent unlike learned bases.

Building on USB, the **Spectral Transform Unit (STU)** was proposed as a neural layer that uses fixed USB filters with learnable coefficients, providing a lightweight alternative for capturing long-range dependencies (Liu et al., 2024).

SFO bridges *explicit kernel representation* and *Fourier-based* operators: as in kernel-learning methods such as SVD-NO, it learns the kernel via a constrained expansion. Specifically, SFO expands the kernel in the USB and learns only the expansion coefficients. It then evaluates the resulting integral efficiently in the frequency domain, as in Fourier-based models. Conceptually, SFO adapts STU-style USB spectral filtering from sequence modeling to PDE operator learning, yielding a compact global kernel.

## 3. Neural Operator Background

**Operator Learning.** Let  $\mathcal{D} \subset \mathbb{R}^{d_x}$  be a bounded domain. Consider the Hilbert spaces  $\mathcal{A} := L^2(\mathcal{D}; \mathbb{R}^{d_a})$ ,  $\mathcal{U} := L^2(\mathcal{D}; \mathbb{R}^{d_u})$ , and the latent space  $\mathcal{V} := L^2(\mathcal{D}; \mathbb{R}^{d_v})$ . An operator  $\mathcal{G} : \mathcal{A} \rightarrow \mathcal{U}$  maps an input field  $a \in \mathcal{A}$  to a output field  $u = \mathcal{G}(a) \in \mathcal{U}$  (e.g. the PDE solution). Learning  $\mathcal{G}$  from a finite set of samples  $\{(a_j, u_j)\}_{j=1}^N$  with  $u_j = \mathcal{G}(a_j)$ , where  $N$  is the number of samples (Li, 2021).

**Neural Operator Architecture.** A neural operator parameterizes an approximate operator  $\mathcal{G}_\theta : \mathcal{A} \rightarrow \mathcal{U}$ , typically through a composition of lifting, operator layers and projection. While not required for all architectures (e.g. DeepONet

<sup>1</sup><https://anonymous.4open.science/r/STUNO-678F>

(Lu et al., 2021) does not follow this structure), this formulation is common among kernel-based neural operators such as FNO (Li et al., 2021). The operator is written as

$$\mathcal{G}_\theta = Q \circ [\text{layer}_{T-1}(\mathcal{K}_\theta^{T-1})] \circ \dots \circ [\text{layer}_0(\mathcal{K}_\theta^0)] \circ P,$$

where:

- $P : \mathbb{R}^{d_a} \rightarrow \mathbb{R}^{d_v}$  and  $Q : \mathbb{R}^{d_v} \rightarrow \mathbb{R}^{d_u}$  are pointwise maps that lift the input field to a latent representation and project the final latent state back to the output. Specifically,  $v^0(x) = P(a(x))$  and  $u(x) = Q(v^T(x))$ .

- Each layer applies an integral operator  $\mathcal{K}_\theta^t(a) : \mathcal{V} \rightarrow \mathcal{V}$ .
- The operator  $\mathcal{K}_\theta^t(a)$  is defined through a kernel  $\kappa_\theta^t$  by

$$[\mathcal{K}_\theta^t(a)v](x) = \int_{\mathcal{D}} \kappa_\theta^t(x, a(x), x', a(x')) v(x') dx' \quad (1)$$

The choice of parameterization for  $\kappa_\theta^t$  determines the expressive power of the neural operator.

## 4. Universal Spectral Basis (USB)

The *Universal Spectral Basis* (USB) framework of (Hazan et al., 2017) shows that a long-range structure in LDS can be captured using *spectral filters* derived from the Hilbert matrix. Subsequent works extend USB spectral filtering to wider classes of nonlinear dynamics (Dogariu et al., 2025).

**The Hilbert eigenvectors.** The Hilbert matrix is a classical object in numerical analysis. The  $n \times n$  matrix is defined by

$$H_{ij} = \frac{1}{i+j-1}, \quad i, j = 1, \dots, n.$$

Its eigenvectors, denoted  $\{\phi_l\}_{l=1}^n$ , provide a fixed, globally supported orthonormal filter bank on a uniform grid, which we use for parameterizing kernels. Most importantly, these eigenvectors form an orthonormal system that exhibits:

1. *Global*: Each eigenvector spans the entire domain.
2. *Fast spectral decay*: The eigenvalues decay rapidly; beyond roughly 20 modes they are numerically negligible. This allows us to use a small number of modes while capturing the global structure of the signal.
3. *Universality*: Hilbert filters form an  $\ell_2$ -complete basis as  $L \rightarrow n$  (where  $L$  is the number of retained modes).

**Discrete USB filters and their continuous interpretation.** The USB modes  $\{\phi_l\}_{l=1}^n$  are the  $\ell_2$ -orthonormal eigenvectors of  $H$  on the computational grid. Let  $\mathcal{D} = [0, 1]$  be discretized by a uniform grid  $\{x_i\}_{i=1}^n$  with spacing  $\Delta x = 1/n$ . Let  $H^{(n)} \in \mathbb{R}^{n \times n}$  be the Hilbert matrix  $H_{ij}^{(n)} = \frac{1}{i+j-1}$ . We define the associated piecewise-constant functions

$$\phi_l^{(n)}(x) := \phi_l[i] \quad \text{for } x \in [x_i, x_{i+1}).$$

Then  $\{\phi_l^{(n)}\}$  is orthogonal in  $L^2(\mathcal{D})$ .

**Spectral Transform Unit (STU).** STU layers leverage the USB basis for sequence modeling by mixing USB modes with learned coefficients (Agarwal et al., 2023). Concretely, given an input signal  $v$ , an STU layer can be written as

$$\text{STU}(v) = \sum_{l=1}^L \theta_l \langle v, \phi_l \rangle, \quad (2)$$

where  $\{\theta_l\}_{l=1}^L$  are learned coefficients, and  $\langle \cdot, \cdot \rangle$  denotes the inner product. (In the continuous form, the  $L^2(\mathcal{D})$  inner product is  $\langle v, \phi_l^{(n)} \rangle = \int_{\mathcal{D}} v(x) \phi_l^{(n)}(x) dx$ .)

Flash-STU (Liu et al., 2024) further composes STU layers with nonlinearities to increase expressivity.

Although USB was originally introduced for temporal sequences, the Hilbert basis is defined purely by index structure and does not rely on temporal semantics; consequently, the same modes can also be applied over spatial grid axes.

### 4.1. LDS Structure in PDE Kernels

We consider integral operators on  $\mathcal{D} \subset \mathbb{R}$ ,

$$(\mathcal{K}v)(x) = \int_{\mathcal{D}} \kappa(x, x') v(x') dx'.$$

A special case is a shift-invariant kernel  $\kappa(x, x') = g(x - x')$  with geometric (exponential) decay:

$$\kappa(x, x') = g(x - x') = c \rho^{|x-x'|}, \quad |\rho| < 1. \quad (3)$$

On a uniform grid, (3) exhibits stable LDS behavior along the *spatial* index: influence depends only on the offset  $|x - x'|$  and decays exponentially with distance. This is where truncated USB spectral filtering yields rapidly decaying expansion coefficients and accurate low-mode approximations (App. G); moreover, it remains effective even near marginal stability ( $|\rho| \approx 1$ ) (Hazan et al., 2017).

**Geometric kernels from local stencils.** A representative case where this geometric decay arises is the inverse of a *three-point stencil* Toeplitz operator. Let  $K$  be the Toeplitz operator  $(Kv)_i = b v_{i-1} + a v_i + b v_{i+1}$ ,  $a > 2|b|$ .  $K$  is invertible and the entries of  $K^{-1}$  decay geometrically with  $|i - j|$  (see Appendix G). Such systems arise from standard second-order finite-difference discretizations of common 1D PDE resolvents (e.g., implicit diffusion) (App. G).

**Implication for USB truncation.** Let  $g \in \mathbb{R}^N$  be the discretized kernel and expand it in the USB basis  $\{\phi_\ell\}_{\ell=1}^N$ :

$$g[i] = \sum_{\ell=1}^N \theta_\ell \phi_\ell[i], \quad \text{so that} \quad \tilde{g}_L[i] = \sum_{\ell=1}^L \theta_\ell \phi_\ell[i]$$

is the rank- $L$  (USB-truncated) approximation. Since geometric Toeplitz kernels correspond to stable 1D LDS along

the spatial index, prior USB results imply their energy concentrates on low-index USB modes, so the coefficients  $\{\theta_\ell\}$  decay rapidly. Consequently, truncation achieves small error. Concretely, as shown in Theorem. G.1, for any target accuracy  $\epsilon > 0$  there exists an  $L$  such that

$$\|g - \tilde{g}_L\|_2 \leq \epsilon, \quad L = \tilde{\mathcal{O}}(\log(1/\epsilon)).$$

Accordingly, SFO constrains  $\kappa$  to the leading USB modes. For nonlinear PDEs, intuitively, the pre-SFO projection is a Koopman lift, making feature-space dynamics near-linear.

## 5. The Spectral Filtering Operator (SFO)

### 5.1. SFO Theory and Architecture

**Integral Layer Reformulation.** Let  $\mathcal{D} \subset \mathbb{R}$  be a bounded spatial domain and let  $a: \mathcal{D} \rightarrow \mathbb{R}^{d_a}$  denote an input field, recall the generic integral layer (Eq.1)

$$[\mathcal{K}_\theta(a) v](x) = \int_{\mathcal{D}} \kappa_\theta(x, a(x), x', a(x')) v(x') dx',$$

In SFO, the kernel  $\kappa_\theta$  is parameterized by a truncated expansion in the top  $L$  Hilbert modes. Since these modes are globally supported, they provide a compact basis for nonlocal interactions, and the kernel acts through only  $L$  global components. Input dependence is introduced by the lifting map and the nonlinear latent updates across layers. Figures 1 and 2 provide an overview.

**A Spectral Parameterization: Scalar Case.** Consider the scalar setting, where  $v^t: \mathcal{D} \rightarrow \mathbb{R}$  and  $\kappa_\theta$  is scalar-valued. Following the spectral filtering framework, SFO constrains  $\kappa_\theta$  to lie in the span of a fixed global orthonormal system given by the Hilbert (USB) filters on a uniform grid. Let  $\{\phi_l\}_{l \geq 1}$  denote these filters. We define the kernel as

$$\kappa_\theta(x, x') = \sum_{l=1}^{\infty} \theta_l \phi_l(x - x'), \quad (x, x') \in \mathcal{D} \times \mathcal{D}, \quad (4)$$

with spectral coefficients  $\theta_l \in \mathbb{R}$ . Motivated by the rapid USB coefficient decay (Sec. 4.1), we parameterize  $\kappa_\theta$  by a truncated expansion in the top  $L$  Hilbert modes.

$$\kappa_{\theta, L}(x, x') = \sum_{l=1}^L \theta_l \phi_l(x - x'). \quad (5)$$

We assume periodic boundary conditions, i.e.,  $\phi_l(x - x')$  is interpreted modulo the grid size (equivalently, FFT evaluation in Eq. (8) performs circular convolution).

**Update Equation.** Inserting (5) into the generic integral layer (1) gives

$$(\mathcal{K}_\theta v)(x) = \int_{\mathcal{D}} \sum_{l=1}^L \theta_l \phi_l(x - x') v(x') dx'. \quad (6)$$

which simplifies to

$$(\mathcal{K}_\theta v)(x) = \sum_{l=1}^L \theta_l \int_{\mathcal{D}} \phi_l(x - x') v(x') dx'. \quad (7)$$

**Integral Computation.** Constraining  $\kappa_{\theta, L}(x, x') = g(x - x')$  makes the operator shift-invariant, so (7) reduces to a convolution. We evaluate this convolution efficiently using the Fast Fourier Transform (FFT), denoted by  $\mathcal{F}$ .

$$(\mathcal{K}_\theta v)(x) = \sum_{l=1}^L \theta_l \mathcal{F}^{-1}(\mathcal{F}(\phi_l) \odot \mathcal{F}(v))(x), \quad (8)$$

where  $\odot$  denotes elementwise multiplication.

**Extension to Vector-Valued Fields.** For vector-valued fields  $v: \mathcal{D} \rightarrow \mathbb{R}^d$ , the operator uses matrix-valued kernels

$$\kappa: \mathcal{D} \times \mathcal{D} \rightarrow \mathbb{R}^{d \times d}.$$

In this setting, the global set of  $L$  Hilbert modes  $\{\phi_l\}_{l=1}^L$  is shared across channels, and each mode is equipped with a learned channel-mixing matrix  $\Theta_l \in \mathbb{R}^{d \times d}$ . Replacing the scalar weights  $\theta_l \in \mathbb{R}$  from the single-channel case yields

$$\kappa(x, x') = \sum_{l=1}^L \Theta_l \phi_l(x - x'). \quad (9)$$

The diagonal of  $\Theta_l$  controls per-channel weights, while the off-diagonal entries encode cross-channel couplings. The resulting update rule becomes

$$(\mathcal{K}_\theta v)(x) = \sum_{l=1}^L \Theta_l \mathcal{F}^{-1}(\mathcal{F}(\phi_l) \odot \mathcal{F}(v))(x). \quad (10)$$

**Extension to high-dimensional grids.** For a PDE defined on an  $M$ -dimensional grid with axes  $x_1, \dots, x_M$ , the high-dimensional modes  $\{\phi_l(x_1, \dots, x_M)\}_{l=1}^L$  are obtained via a separable *tied-index* tensor product of the 1D modes:

$$\phi_l(x_1, \dots, x_M) = \prod_{m=1}^M \phi_l(x_m). \quad (11)$$

This yields  $L$  globally supported  $M$ -dimensional modes, where the same index  $l$  is shared across all axes (coupling them through a common mode). We ablate the more expressive  $L^M$  *multi-index* construction in Section 7.1.

**Convergence as  $L \rightarrow \infty$ .** In SFO we restrict to kernels  $\kappa(x, x') = g(x - x')$  with  $g \in L^2(\mathcal{D})$ . Let  $\{\phi_l\}_{l \geq 1}$  be an orthonormal basis, and define  $g_L := \sum_{l=1}^L \theta_l \phi_l$ . Then  $\kappa_L(x, x') := g_L(x - x')$  is the orthogonal projection of  $g$  onto  $\text{span}\{\phi_1, \dots, \phi_L\}$ , hence  $\|g - g_L\|_{L^2} \rightarrow 0$  as  $L \rightarrow \infty$ .

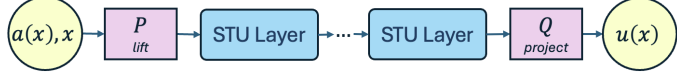


Figure 1. SFO architecture. The input field  $(a(x), x)$ , is lifted by a map  $P$  to a latent representation  $v^0$ . The latent field is updated by  $T$  stacked STU layers, each applying an operator  $\mathcal{K}$ . Finally, a projection  $Q$  maps the last latent state  $v^T$  back to the solution field  $u(x)$ .

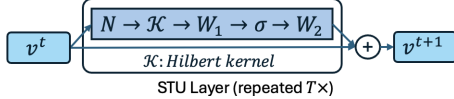


Figure 2. STU layer: the current state  $v^t$  is normalized ( $N$ ), passed through the operator  $\mathcal{K}$ , then through a linear transformation with a nonlinearity, and added back to  $v^t$ . The operator  $\mathcal{K}$  itself is implemented via STU in the Fourier domain using the top  $L$  Hilbert eigenmodes  $\{\phi_l\}_{l=1}^L$ ,  $\mathcal{K}v^t = \sum_{l=1}^L \Theta_l \mathcal{F}^{-1}(\hat{v}^t \odot \hat{\phi}_l)$ .

In the  $M$ -dimensional tied-index extension, we obtain  $L$  separable modes, and as  $L \rightarrow \infty$  the approximation converges in  $L^2$  to the best tied-index separable approximation.

**Discrete Form.** Let  $\{x_j\}_{j=1}^n$  be a uniform grid on  $\mathcal{D}$  with spacing  $\Delta x$ . The integral operator for the vector-valued STU layer is approximated by

$$(\mathcal{K}_\theta v^t)(x_i) = \sum_{l=1}^L \Theta_l \sum_{j=1}^n \phi_l(x_i - x_j) v^t(x_j) \Delta x, \quad (12)$$

$$i = 1, \dots, n,$$

The inner sum is a discrete convolution between the filter  $\phi_l$  and  $v^t$ , which can be computed efficiently via the Discrete Fourier Transform (DFT) denoted by  $\mathcal{F}_d$ . Defining  $\hat{\phi}_l = \mathcal{F}_d(\phi_l)$  and  $\hat{v}^t = \mathcal{F}_d(v^t)$ , the update can be written as

$$(\mathcal{K}_\theta v^t)(x_i) = \sum_{l=1}^L \Theta_l \left[ \mathcal{F}_d^{-1}(\hat{\phi}_l \odot \hat{v}^t) \right]_i, \quad i = 1, \dots, n. \quad (13)$$

**Direct Factor Parameterization.** Rather than first learning an unconstrained kernel  $\kappa$  and then factorizing it, we directly parameterize  $\kappa$  in terms of its STU components. Specifically, the learnable parameters are the spectral coefficients  $\{\Theta_l\}_{l=1}^L$  associated with the Hilbert eigenmodes.

**Iterative Updates.** Kernel-based neural operators follow an iterative update pattern in which the latent field evolves across layers (Li et al., 2021). The input  $a(x)$  is first lifted into a high-dimensional representation  $v^0(x) = P((a(x), x))$ , where  $P$  is a linear map. After  $T$  updates, the final state  $v^T$  is projected back to the solution space by  $Q$ , yielding  $u(x) = Q(v^T(x))$ .

In SFO, each layer  $t = 0, \dots, T-1$  first normalizes the latent field, then processes it with an STU operator  $\mathcal{K}_\theta^t$ , and finally applies the residual MLP nonlinearity used in Flash-STU (Liu et al., 2024).

We denote the operator output by  $\tilde{v}^t(x) = \mathcal{K}_{\theta^t}(N(v^t))(x)$ , where  $N(\cdot)$  is a Layer Normalization applied to the latent field, and we update  $v^{t+1}(x)$  accordingly

$$v^{t+1}(x) = v^t(x) + W_2^t \sigma(W_1^t \tilde{v}^t(x)).$$

## 5.2. Expressivity

SFO attains high expressivity by expanding the kernel in a fixed orthonormal Hilbert (USB) basis and learning only the expansion coefficients. The only approximation is truncation to the top  $L$  modes; empirically, the Hilbert spectrum decays rapidly, so modes beyond  $l \approx 20$  are often negligible, and a small rank suffices for an accurate and efficient global kernel. While formal guarantees apply to PDEs whose Green’s function exhibits an LDS-structure (App. G), we find the same structure effective across a broad range of PDE operator-learning benchmarks (Fig. 3).

This design contrasts with prior approaches. Unlike SVD-NO, which learns a data-adaptive low-rank kernel (both basis and rank are learned) and can be more sensitive to data coverage, SFO fixes the kernel basis and learns only the expansion coefficients. FNO also fixes a basis (Fourier), but its low-frequency truncation with learned multipliers imposes an explicit smoothness bias. In contrast, SFO truncates only for efficiency: due to rapid Hilbert spectral decay, omitted modes are typically negligible. Finally, unlike graph-based operators where locality requires deep stacking and can cause oversmoothing, the global support of Hilbert modes enables global information propagation in a single layer.

## 5.3. Computational Complexity

**Time Complexity.** Let  $n$  be the number of grid points,  $d$  the latent dimension, and  $L$  the number of modes. An STU layer applies  $L$  fixed filters  $\{\phi_l\}_{l=1}^L$  in the Fourier domain. We compute one FFT of the  $d$ -channel field  $v^t$ , costing  $O(dn \log n)$ , and multiply by the precomputed transforms  $\{\mathcal{F}(\phi_l)\}_{l=1}^L$ , costing  $O(Ldn)$ . Rather than performing  $L$  inverse FFTs, we apply  $\Theta_l \in \mathbb{R}^{d \times d}$  and sum over modes directly in the frequency domain (by linearity of  $\mathcal{F}$ ), costing  $O(Ld^2n)$ . We then compute one inverse FFT to return to the spatial domain,  $O(dn \log n)$ . (Eq. (13) is written mode-wise for clarity, but evaluated using a single inverse FFT after aggregating all modes.) Thus, the time per layer is

$$O(dn \log n + Ldn + Ld^2n).$$

Empirical runtimes are reported in App. D, where SFO is comparable to FNO.

**Memory Complexity.** An STU layer stores the input and output latent fields of size  $d \times n$ , i.e.,  $O(dn)$ . FFT computation allocates buffers of comparable size, so the peak memory remains  $O(dn)$ . The precomputed filters  $\{\mathcal{F}(\phi_l)\}_{l=1}^L$  require  $O(Ln)$ . The learnable  $L$  matrices  $\{\Theta_l\}_{l=1}^L$  contribute  $O(Ld^2)$ . Thus, the memory complexity is

$$O(dn + Ln + Ld^2).$$

## 6. Empirical Evaluation

### 6.1. Experimental Methodology

The experiments quantify how well SFO generalizes across diverse benchmarks and compared to SOTA baselines. Performance is reported as the *mean  $L_2$  relative error (%)*:

$$L_2 (\%) = 100 \times \frac{1}{N} \sum_{i=1}^N \frac{\|u_i - \hat{u}_i\|_2}{\|u_i\|_2} \quad (14)$$

where  $\|\cdot\|_2$  is the Euclidean norm. This metric is standard in operator-learning benchmarks (Wei et al., 2024).

### 6.2. Baseline Models

We compare SFO to seven baselines: SVD-NO, DeepONet, FNO, UNO, MPNN, PINO, and UNet, spanning all neural-operator categories in Sec. 2. The representatives for each category are the models in PDENNEval (Wei et al., 2024), a survey of neural operators for PDEs, and SVD-NO.

### 6.3. Datasets

The following six PDE datasets are taken from (Wei et al., 2024) and processed exactly as in the survey:

#### 1D Allen-Cahn.

$\partial_t u - \epsilon \partial_{xx} u + 5u^3 - 5u = 0$ ,  $\epsilon = 10^{-4}$  on  $(-1, 1) \times (0, 1]$ .  
Input: Initial conditions  $u(x, 0) \in \mathbb{R}^{256}$ .  
Output: Full solution  $u(x, t) \in \mathbb{R}^{256 \times 101}$ .

#### 1D Diffusion-Reaction.

$\partial_t u - 0.5 \partial_{xx} u - u(1-u) = 0$  on  $(0, 1) \times (0, 1]$  (periodic).  
Input: Initial conditions  $u(x, 0) \in \mathbb{R}^{256}$ .  
Output: Full solution  $u(x, t) \in \mathbb{R}^{256 \times 101}$ .

#### 1D Diffusion-Sorption.

$\partial_t u - \frac{D}{R(u)} \partial_{xx} u = 0$  on  $(0, 1) \times (0, 1]$   
Boundary conditions:  $u(0, t) = 1$ ,  $u_x(1, t) = D^{-1}u(1, t)$   
with  $D = 5 \times 10^{-4}$  and Freundlich  $R(u)$ .  
Input: Initial conditions  $u(x, 0) \in \mathbb{R}^{256}$ .  
Output: Full solution  $u(x, t) \in \mathbb{R}^{256 \times 101}$ .

#### 1D Cahn-Hilliard.

$\partial_t u - \partial_{xx}(10^{-2}(u^3 - u) - 10^{-6}\partial_{xx}u) = 0$ ,  
 $(x, t) \in (-1, 1) \times (0, 1]$   
Boundary conditions:

$$u(-1, t) = u(1, t), \partial_x u(-1, t) = \partial_x u(1, t)$$

Input: Initial conditions  $u(x, 0) \in \mathbb{R}^{1024}$ .

Output: Full solution  $u(x, t) \in \mathbb{R}^{1024 \times 101}$ .

#### 2D Shallow Water.

$$\partial_t h + \partial_x(hu) + \partial_y(hv) = 0$$

$$\partial_t(hu) + \partial_x(u^2h + \frac{1}{2}g_rh^2) + g_rh\partial_xb = 0$$

$$\partial_t(hv) + \partial_y(v^2h + \frac{1}{2}g_rh^2) + g_rh\partial_yb = 0.$$

Input:  $(h(x, y, 0), b(x, y)) \in \mathbb{R}^{128 \times 128}$ .

Output: Solution  $(h, u, v) \in \mathbb{R}^{128 \times 128 \times 101}$ .

#### 3D Maxwell's Equations.

$$\nabla \cdot E = 0, \nabla \cdot H = 0,$$

$$\nabla \times E = -\frac{\mu}{c} \frac{\partial H}{\partial t}, \nabla \times H = \frac{\epsilon}{c} \frac{\partial E}{\partial t}.$$

with  $\epsilon = 10$ ,  $\mu = 1$ . The system has 6 time-evolving field components  $(E_x, E_y, E_z, H_x, H_y, H_z)$ .

Input:  $(E(x, y, z, t), H(x, y, z, t)) \in \mathbb{R}^{32 \times 32 \times 32 \times 2 \times 6}$ .

Output:  $(E(x, y, z, t), H(x, y, z, t)) \in \mathbb{R}^{32 \times 32 \times 32 \times 8 \times 6}$ .

Together, these datasets span reaction-diffusion (Diffusion-Reaction/Sorption, Allen-Cahn, Cahn-Hilliard), fluid dynamics (Shallow Water), and electromagnetics (Maxwell), providing a broad test bed. Moreover, local shifted operators underlying Allen-Cahn, Reaction-Diffusion, and Cahn-Hilliard have integral kernels of LDS structure in the spatial axis (App. G). We extend the intuition to nonlinear PDEs via feature-space linearization induced by the pre-SFO projection.

Each dataset provides pairs  $\{(a_j, u_j)\}_{j=1}^N$  of input fields  $a_j$  (initial conditions) and solutions  $u_j$  (full trajectories).

### 6.4. Experimental Setup

Experiments were conducted on an NVIDIA A30 PCIe GPU. Following (Koren et al., 2025), we trained each model for 500 epochs (200 for Shallow Water). Each dataset of input-solution pairs  $\{(a_j, u_j)\}_{j=1}^N$  was split into 90% training and 10% held-out data for validation/testing. We optimized the mean  $L_2$  relative error in Eq. 14 using the ADAM optimizer with learning rate  $10^{-3}$ . All time steps were learned jointly.

**Hyperparameter Tuning.** App B lists the selected hyperparameters. For SFO, we tune only the method-specific hyperparameters: the rank  $L$  (number of Hilbert modes) and the lifting dimension  $d$  (mapping  $a$  to  $v$ ). We use  $\sigma = \text{gelu}$  and  $T = 4$  operator layers, following (Koren et al., 2025).

We tune  $L$  and  $d$  via a grid search over  $L \in \{16, 20\}$  and  $d \in \{32, 64, 128\}$ . We restrict  $L$  to  $\{16, 20\}$  since the Hilbert spectrum decays rapidly and performance saturates around  $L \approx 20$  (Fig. 3). Fig. 4 and Table 5 ablate  $L$  and  $d$ .

**Baseline Hyperparameters.** For baselines we used the data-specific tuned configurations from PDENNEval (Wei et al., 2024) and SVD-NO (Koren et al., 2025), and trained them under the same protocol as SFO (data splits, learning

rate, epochs, etc.). As a sanity check, we ran a local sweep around the PDENNEval settings (e.g., width/modes) and observed no improvement over the reported configurations.

## 7. Results

The experimental results in Table 1 compare SFO against seven SOTA operator-learning methods on six PDE benchmarks using the mean  $L_2$  relative error (%) (Eq. 14). For Diffusion-Sorption, the absolute differences between methods are small (on the order of  $10^{-3}$ ), so we report a scaled value  $10 \times L_2(\%)$  to make them easier to read.

SFO achieves SOTA performance: it obtains error reductions relative to the best-performing baseline on each PDE, with improvements of 28.57% on Allen-Cahn, 0.9% on Diffusion-Sorption, 33.33% on Diffusion-Reaction, 38.46% on Cahn-Hilliard, 2.56% on Shallow Water, and 18.81% on Maxwell’s Equations. These results indicate that SFO combines strong accuracy with consistent generalization across diverse PDEs. Training times are reported in Appendix D, where SFO is comparable to FNO.

Consistent with prior work (Wei et al., 2024), Maxwell shows higher errors due to its high-dimensional wave dynamics. DeepONet and UNet also lag the strongest baselines (Wei et al., 2024): UNet is not tailored to operator learning, and DeepONet’s branch–trunk factorization can struggle with structured spatiotemporal dynamics.

**Significance of Results.** To assess robustness, each experiment was repeated 10 times with different random seeds. For each PDE we report the sample mean and its 95% confidence interval. These statistics are presented in Table 1.

**Learned Hilbert coefficients.** To better understand the inductive bias of the USB underlying our truncation, we compute the Frobenius norm  $\|\Theta_l\|_F$  for each mode  $l$  in every STU layer and average across layers. Fig. 3 shows that coefficients concentrate on low-index modes and decay with  $l$ , indicating SFO relies on few global modes and supporting a low-rank truncation  $L$ . Additional results across all PDEs are reported in App. A. While our formal guarantees apply to settings where the Green’s kernel admits an LDS structure (App. G), Fig. 3 suggests that a similar low-mode bias emerges empirically across diverse PDEs.

**Compact parameterization.** Averaged over 1D, 2D, and 3D benchmarks, SFO uses fewer learnable parameters than SVD-NO and is orders of magnitude smaller than DeepONet, UNO, and UNet. Compared to FNO and PINO, SFO is slightly smaller in 1D and 2D and over an order of magnitude smaller in 3D (App. C, Table 7).

**Largest gains on PDEs with LDS-structure kernels.** SFO achieves its largest relative improvements on Allen-Cahn, Diffusion-Reaction, and Cahn-Hilliard. Although these

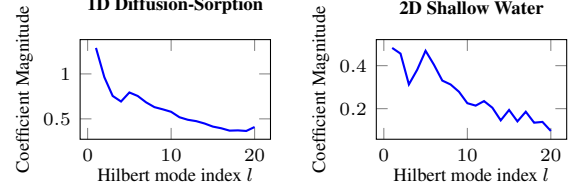


Figure 3. Magnitude of learned Hilbert spectral coefficients vs. mode index  $l$ . We plot the Frobenius norms  $\|\Theta_l\|_F$  averaged across STU layers. Coefficients decay with  $l$ , indicating SFO concentrates most of its capacity on a few low-index global modes.

PDEs are nonlinear, the corresponding lifted operators exhibit geometrically decaying Green’s kernels (App. G).

### 7.1. Ablation Studies

To evaluate the contribution of the key architectural choices in SFO, we conduct the following ablation studies.

**Fixed Orthogonal Basis.** To isolate the effect of USB, we replace the Hilbert basis in SFO with other fixed global orthonormal bases: Fourier, Chebyshev, and a random orthogonal basis (the  $Q$  factor from QR of an i.i.d. Gaussian matrix), keeping all settings fixed (including rank  $L$ ). Table 2 shows USB leads on 4/6 benchmarks, ties Chebyshev on Allen-Cahn, and is slightly worse on Cahn-Hilliard; Fourier and random bases consistently underperform. Since SFO uses only  $L$  modes, this compares truncated bases under the same mode budget (Fourier and Chebyshev are complete only with all  $n$  modes), suggesting USB’s leading modes capture more task-relevant global structure.

**GLU vs. MLP.** Inspired by a future-work suggestion in Flash-STU (Liu et al., 2024), we replace the update  $v_t \rightarrow v_{t+1}$  with a GLU gate:  $G^t = W_g^t \mathcal{K}_\theta^t(v^t)$ ,  $V^t = W_v^t \mathcal{K}_\theta^t(v^t)$ ,

$$v^{t+1}(x) = v^t(x) + \sigma(G^t(x)) \odot V^t(x),$$

with  $\odot$  the Hadamard product.

The results in Table 3 show that the performance is similar, suggesting that the model’s primary strength comes from the STU kernel itself, rather than the specific layer connections.

**Extension to High-Dimensional Grids ( $L$  vs.  $L^M$  modes).** For PDEs on an  $M$ -dimensional grid, one can extend the 1D Hilbert modes  $\{\phi_l\}_{l=1}^L$  to  $M$  dimensions in two natural ways: *multi-index* and *tied-index*. In the *multi-index* formulation, we form a separable mode for every index tuple  $I = (i_1, \dots, i_M) \in \{1, \dots, L\}^M$ :

$$\Phi_I(x_1, \dots, x_M) = \prod_{m=1}^M \phi_{i_m}(x_m),$$

yielding  $L^M$  modes. In contrast, the *tied-index* formulation in Eq. 11 uses  $L$  modes. Since the per-layer time and memory scale linearly with the number of modes  $K$ , the

Table 1. Mean  $L_2$  relative error (%). Best results are in **bold**, second-best are underlined. The  $\pm$  values denote 95% confidence intervals. In Diffusion-Sorption, the gaps between methods are on the order of  $10^{-3}$ ; so we report a scaled value  $10 \times L_2(\%)$  for readability.

Category	SFO	SVD-NO	FNO	UNO	PINO	MPNN	DeepONet	UNet
	<i>Ours</i>	<i>SVD Kernel</i>	<i>Fourier</i>	<i>Fourier</i>	<i>PINN, Fourier</i>	<i>Graph (Local)</i>	<i>DeepONet</i>	<i>Neural surrogate</i>
1D Allen-Cahn	<b>0.05</b> $\pm 0.012$	<u>0.07</u> $\pm 0.007$	0.08 $\pm 0.001$	0.30 $\pm 0.013$	0.08 $\pm 0.001$	0.33 $\pm 0.009$	16.53 $\pm 0.230$	68.93 $\pm 0.954$
1D Diffusion-Sorption	<b>1.08</b> $\pm 0.006$	<u>1.09</u> $\pm 0.002$	1.09 $\pm 0.001$	1.10 $\pm 0.001$	1.09 $\pm 0.001$	2.86 $\pm 0.004$	1.14 $\pm 0.001$	12.285 $\pm 0.002$
1D Diffusion-Reaction	<b>0.22</b> $\pm 0.021$	<u>0.33</u> $\pm 0.010$	0.39 $\pm 0.014$	0.40 $\pm 0.001$	0.43 $\pm 0.014$	0.39 $\pm 0.015$	0.61 $\pm 0.001$	6.70 $\pm 0.053$
1D Cahn-Hilliard	<b>0.08</b> $\pm 0.005$	0.47 $\pm 0.037$	<u>0.13</u> $\pm 0.004$	0.56 $\pm 0.013$	0.16 $\pm 0.010$	0.59 $\pm 0.011$	8.86 $\pm 0.149$	76.81 $\pm 5.21$
2D Shallow Water	<b>0.38</b> $\pm 0.088$	<u>0.39</u> $\pm 0.042$	0.49 $\pm 0.022$	0.52 $\pm 0.042$	0.46 $\pm 0.002$	0.50 $\pm 0.031$	1.11 $\pm 0.235$	10.93 $\pm 0.706$
3D Maxwell	<b>40.85</b> $\pm 0.103$	63.56 $\pm 0.020$	<u>50.32</u> $\pm 0.031$	50.41 $\pm 0.019$	56.08 $\pm 0.1273$	74.45 $\pm 0.684$	86.12 $\pm 0.596$	63.69 $\pm 0.072$

Table 2. Mean  $L_2$  relative error (%) vs. fixed orthonormal kernel basis. In Diffusion-Sorption, we report  $10 \times L_2(\%)$  for readability.

	SFO	Fourier	Chebyshev	Random
1D Allen-Cahn	<b>0.05</b> $\pm 0.01$	0.17 $\pm 0.01$	<b>0.05</b> $\pm 0.03$	0.16 $\pm 0.01$
1D Diff. Sorption	<b>1.08</b> $\pm 0.01$	1.13 $\pm 0.02$	<u>1.12</u> $\pm 0.01$	1.14 $\pm 0.00$
1D Diff. Reaction	<b>0.22</b> $\pm 0.02$	<u>0.24</u> $\pm 0.03$	0.24 $\pm 0.02$	<u>0.24</u> $\pm 0.02$
1D Cahn-Hilliard	<u>0.08</u> $\pm 0.01$	0.12 $\pm 0.01$	<b>0.07</b> $\pm 0.01$	0.13 $\pm 0.00$
2D Shallow Water	<b>0.38</b> $\pm 0.09$	<u>0.57</u> $\pm 0.06$	0.58 $\pm 0.04$	0.61 $\pm 0.05$
3D Maxwell	<b>40.9</b> $\pm 0.10$	<u>44.4</u> $\pm 0.10$	44.5 $\pm 0.16$	44.8 $\pm 0.44$

Table 3. Mean  $L_2$  relative error (%) for GLU vs. MLP ablation. In Diffusion-Sorption, we report  $10 \times L_2(\%)$  for readability.

	SFO	SFO - GLU Variant
1D Allen-Cahn	<b>0.05</b> $\pm 0.012$	<b>0.05</b> $\pm 0.006$
1D Diffusion-Sorption	<b>1.08</b> $\pm 0.006$	<b>1.08</b> $\pm 0.001$
1D Diffusion-Reaction	<b>0.22</b> $\pm 0.021$	0.23 $\pm 0.030$
1D Cahn-Hilliard	<b>0.08</b> $\pm 0.005$	<u>0.09</u> $\pm 0.012$
2D Shallow Water	<u>0.38</u> $\pm 0.088$	<b>0.37</b> $\pm 0.091$
3D Maxwell	<u>40.85</u> $\pm 0.103$	<b>38.55</b> $\pm 0.075$

multi-index choice scales as  $K = L^M$  and thus becomes exponential in  $M$ , while the tied-index choice keeps  $K = L$ .

To keep the multi-index experiment tractable, we use  $L = 6$  ( $L^2 = 36$ ,  $L^3 = 216$ ). Table 4 shows that multi-index filters degrade performance on 2D Shallow Water and 3D Maxwell despite  $3.8\times$  and  $14.9\times$  more parameters. We hypothesize that the per-layer MLP already captures cross-axis interactions, making the  $L^M$  extension redundant. We therefore adopt the tied-index formulation; while multi-index bases are more expressive in principle, our results show that accuracy gains, if any, do not justify the added parameters.

Table 4. Mean  $L_2$  relative error (%) for tied-index vs. multi-index.

	$L$	Tied-index	$L^M$	Multi-index
2D Shallow Water	6	0.61 $\pm 0.10$	36	0.65 $\pm 0.08$
# Parameters		176,677		668,197
3D Maxwell	6	53.78 $\pm 1.10$	216	56.14 $\pm 2.83$
# Parameters		61,960		922,120

**Effect of STU Rank  $L$ .** Fig. 4 plots test loss versus STU rank  $L$ . As  $L$  increases from 4 to 32, the loss drops rapidly for small ranks ( $L \approx 4\text{--}16$ ) and then plateaus for higher

ranks ( $L \approx 16\text{--}32$ ). This indicates that the leading functions capture most of the operator structure, so additional modes provide only marginal gains. Hence, moderate ranks achieve near-optimal accuracy with a compact parameterization.

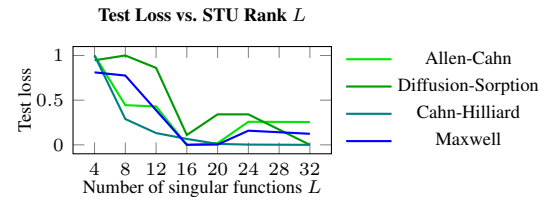


Figure 4. Test loss vs. STU rank  $L$ . The test loss decreases rapidly for small  $L$ , indicating that the leading modes capture most of the structure, and then flattens as additional modes give only marginal gains. All curves are min–max normalized to a common scale.

**Effect of lifting dimension  $d$ .** We sweep the latent width  $d$  with all other hyperparameters fixed. Table 5 shows that performance is relatively stable on most datasets.

Table 5.  $L_2$  relative error (%) vs. lifting dimension  $d$  across PDEs. In Diffusion-Sorption, we report  $10 \times L_2(\%)$  for readability.

	$d = 32$	$d = 64$	$d = 128$
1D Allen-Cahn	0.11	0.05	0.06
1D Diffusion-Sorption	1.12	1.08	1.10
1D Diffusion-Reaction	0.24	0.22	0.27
1D Cahn-Hilliard	0.21	0.08	0.11
2D Shallow Water	0.40	0.38	0.39
3D Maxwell	40.85	55.23	59.56

## 8. Conclusion

We introduced SFO, a neural operator that learns PDE solution maps by parameterizing its kernel in the Universal Spectral Basis (USB) given by Hilbert eigenmodes. Motivated by our theory showing that, for an important subset of PDEs, the Green’s function exhibits LDS structure and is highly compressible, SFO learns only a small set of spectral mixing coefficients over global modes, enabling efficient long-range modeling. Across six PDE benchmarks, SFO achieves SOTA accuracy with up to 40% lower error than the strongest prior method while using fewer parameters. Future work includes extending SFO beyond uniform-grid, shift-invariant FFT evaluation to boundary-aware settings.

## References

Agarwal, N., Suo, D., Chen, X., and Hazan, E. Spectral state space models. *arXiv preprint arXiv:2312.06837*, 2023.

Benzi, M. Decay properties of spectral projectors and functions of banded matrices. *SIAM Review*, 49(4):577–609, 2007.

Bonev, B., Kurth, T., Hundt, C., Pathak, J., Baust, M., Kashinath, K., and Anandkumar, A. Spherical fourier neural operators: Learning stable dynamics on the sphere. In *International Conference on Machine Learning (ICML)*, pp. 2806–2823. PMLR, 2023.

Brandstetter, J., Worrall, D., and Welling, M. Message passing neural pde solvers. In *International Conference on Learning Representations (ICLR)*, 2022.

Cao, Q., Goswami, S., and Karniadakis, G. E. Lno: Laplace neural operator for solving differential equations. *arXiv preprint arXiv:2303.10528*, 2023.

Cao, S. Galerkin transformer. In *2022 Virtual Joint Mathematics Meetings (JMM 2022)*. AMS, 2022.

Demko, S., Moss, W. F., and Smith, P. W. Decay rates for inverses of band matrices. *Mathematics of Computation*, 43(168):491–499, 1984.

Dogariu, E., Brahmbhatt, A., and Hazan, E. Universal learning of nonlinear dynamics. *arXiv preprint arXiv:2508.11990*, 2025.

Eymard, R., Gallouët, T., and Herbin, R. Finite volume methods. *Handbook of numerical analysis*, 7:713–1018, 2000.

Hazan, E. and Singh, K. Introduction to online nonstochastic control. *arXiv preprint arXiv:2211.09619*, 2022.

Hazan, E., Singh, K., and Zhang, C. Learning linear dynamical systems via spectral filtering. In *Advances in Neural Information Processing Systems (NeurIPS)*, 2017.

Herman, R. L. Green’s functions and nonhomogeneous problems. URL <https://people.uncw.edu/hermanr/pde1/pdebook/green.pdf>. Lecture notes.

Koren, N., Mackenbach, R. J., van Sloun, R. J., Radinsky, K., and Freedman, D. Svd-no: Learning pde solution operators with svd integral kernels. *arXiv preprint arXiv:2511.10025*, 2025.

Li, Z. Neural operator: Learning maps between function spaces. In *2021 Fall Western Sectional Meeting*. AMS, 2021.

Li, Z., Kovachki, N., Azizzadenesheli, K., Liu, B., Bhattacharya, K., Stuart, A., and Anandkumar, A. Neural operator: Graph kernel network for partial differential equations. *arXiv preprint arXiv:2003.03485*, 2020.

Li, Z., Kovachki, N., Azizzadenesheli, K., Liu, B., Bhattacharya, K., Stuart, A., and Anandkumar, A. Fourier neural operator for parametric partial differential equations. In *International Conference on Learning Representations (ICLR)*, 2021.

Li, Z., Huang, D. Z., Liu, B., and Anandkumar, A. Fourier neural operator with learned deformations for pdes on general geometries. *Journal of Machine Learning Research*, 24(388):1–26, 2023a.

Li, Z., Kovachki, N., Choy, C., Li, B., Kossaifi, J., Otta, S., Nabian, M. A., Stadler, M., Hundt, C., Azizzadenesheli, K., et al. Geometry-informed neural operator for large-scale 3d pdes. In *Advances in Neural Information Processing Systems (NeurIPS)*, volume 36, pp. 35836–35854, 2023b.

Li, Z., Zheng, H., Kovachki, N., Jin, D., Chen, H., Liu, B., Azizzadenesheli, K., and Anandkumar, A. Physics-informed neural operator for learning partial differential equations. *ACM/JMS Journal of Data Science*, 1(3):1–27, 2024.

Lin, B., Mao, Z., Wang, Z., and Karniadakis, G. E. Operator learning enhanced physics-informed neural networks for solving partial differential equations characterized by sharp solutions. *arXiv preprint arXiv:2310.19590*, 2023.

Liu, Y. I., Nguyen, W., Devre, Y., Dogariu, E., Majumdar, A., and Hazan, E. Flash stu: Fast spectral transform units. *arXiv preprint arXiv:2409.10489*, 2024.

Lu, L., Jin, P., and Karniadakis, G. E. Deeponet: Learning nonlinear operators for identifying differential equations based on the universal approximation theorem of operators. *Nature Machine Intelligence*, 3(3):218–229, 2021.

Ma, Q., Zhao, P., Wang, S., and Song, T. Deep parallel spectral neural operators for solving partial differential equations with enhanced low-frequency learning capability. *arXiv preprint arXiv:2409.19976*, 2024.

Morton, K. W. and Mayers, D. F. *Numerical solution of partial differential equations: an introduction*. Cambridge university press, 2005.

Rahman, M. A., Ross, Z. E., and Azizzadenesheli, K. U-no: U-shaped neural operators. *Transactions on Machine Learning Research*, 2023.

Raonic, B., Molinaro, R., De Ryck, T., Rohner, T., Bartolucci, F., Alaifari, R., Mishra, S., and de Bézenac, E.

Convolutional neural operators for robust and accurate learning of pdes. In *Advances in Neural Information Processing Systems (NeurIPS)*, volume 36, pp. 77187–77200, 2023.

Reddy, J. An introduction to the finite element method, 1993.

Tang, W. and Lin, Z. Global gyrokinetic particle-in-cell simulation. In *Exascale Scientific Applications*, pp. 507–528. Chapman and Hall/CRC, 2017.

Tran, A., Mathews, A., Xie, L., and Ong, C. S. Factorized fourier neural operators. In *International Conference on Learning Representations (ICLR)*, 2023.

Tripura, T. and Chakraborty, S. Wavelet neural operator: a neural operator for parametric partial differential equations. *Computer Methods in Applied Mechanics and Engineering*, 404:115783, 2023.

Wei, P., Liu, M., Cen, J., Zhou, Z., Chen, L., and Zou, Q. Pdenneval: A comprehensive evaluation of neural network methods for solving pdes. In *Thirty-Third International Joint Conference on Artificial Intelligence (IJCAI)*, 2024.

Wen, G., Li, Z., Azizzadenesheli, K., Anandkumar, A., and Benson, S. M. U-fno—an enhanced fourier neural operator-based deep-learning model for multiphase flow. *Advances in Water Resources*, 163:104180, 2022.

Xiong, W., Huang, X., Zhang, Z., Deng, R., Sun, P., and Tian, Y. Koopman neural operator as a mesh-free solver of non-linear partial differential equations. *arXiv preprint arXiv:2301.10022*, 2023.

Zhu, M., Feng, S., Lin, Y., and Lu, L. Fourier-deepnet: Fourier-enhanced deep operator networks for full waveform inversion with improved accuracy, generalizability, and robustness. *Computer Methods in Applied Mechanics and Engineering*, 416:116306, 2023.

## A. Analysis of learned Hilbert coefficients.

We analyze the learned Hilbert spectral coefficients across PDE benchmarks. For each STU layer, we compute the Frobenius norm  $\|\Theta_l\|_F$  of the coefficient matrix associated with mode  $l$  and average across layers. Figure 5 shows that across 5/6 cases, the coefficients place more weight on low-index modes and decrease with increasing  $l$ , providing additional evidence that SFO relies primarily on a small set of global Hilbert modes.

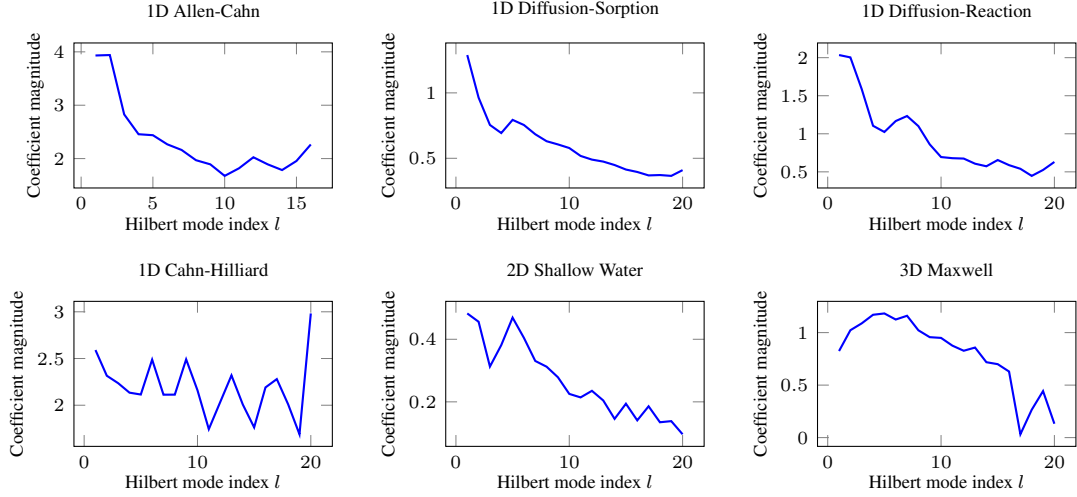


Figure 5. Average magnitude of learned Hilbert spectral coefficients across benchmarks. For each STU layer, we compute the Frobenius norm  $\|\Theta_l\|_F$  of the coefficient matrix associated with mode  $l$  and average across layers. The learned coefficients emphasize low-index modes, supporting the use of a truncated Hilbert expansion.

## B. Hyperparameter Tuning.

Table 6 summarizes the selected hyperparameters. For SFO, we tune only the method-specific parameters: the rank  $L$  (number of Hilbert modes) and the lifting dimension  $d$  (mapping  $a$  to  $v$ ). We fix the activation to  $\sigma = \text{gelu}$  and use  $T = 4$  operator layers, following (Koren et al., 2025).

We select  $L$  and  $d$  via grid search over  $L \in \{16, 20\}$  and  $d \in \{32, 64, 128\}$ . We restrict  $L$  to  $\{16, 20\}$  since the Hilbert spectrum decays rapidly and performance saturates around  $L \approx 20$  (Fig. 3). Fig. 4 and Table 5 report ablations over  $L$  and  $d$ .

Table 6. Selected  $L$  and  $d$  per PDE

	Rank $L$	Lifting Dimension $d$
1D Allen-Cahn	16	64
1D Diffusion-Sorption	20	32
1D Diffusion-Reaction	20	64
1D Cahn-Hilliard	20	64
2D Shallow Water	20	64
3D Maxwell	20	32

## C. Compact Parameter Counts.

We report empirical model size for all baselines. Table 7 summarizes the number of learnable parameters, averaged by PDE dimensionality (1D/2D/3D), providing a compact comparison across problem classes. Overall, SFO is parameter-efficient: it uses fewer parameters than SVD-NO and is orders of magnitude smaller than DeepONet, UNO, and U-Net. Compared to FNO and PINO, SFO is slightly smaller in 1D and 2D and over an order of magnitude smaller in 3D.

Table 7. Average number of learnable parameters by PDE dimension.

	<b>SFO</b>	<b>SVD-NO</b>	<b>DeepONet</b>	<b>FNO and PINO</b>	<b>UNO</b>	<b>UNet</b>
1D	283,413	586,193	3,451,237	300,325	1,097,051	2,711,109
2D	406,053	973,289	429,143,808	478,277	5,984,051	2,711,109
3D	119,304	125,452	52,034,992	3,287,780	90,221,664	22,589,328

## D. Run time

Table 8 reports the average wall-clock training time per epoch (seconds per epoch) across PDE benchmarks under an identical training setup. All methods were trained with the same data splits, optimizer and learning-rate schedule, batch size, and number of gradient updates per epoch. Overall, FNO, UNO, and SFO are among the fastest methods on most benchmarks.

Table 8. Training time per epoch (in seconds) across PDE benchmarks.

	<b>SFO</b>	<b>SVD-NO</b>	<b>DeepONet</b>	<b>FNO</b>	<b>UNO</b>	<b>PINO</b>	<b>UNet</b>
1D Allen-Cahn	2.09	5.87	1.09	1.61	2.06	2.57	2.33
1D Diffusion-Sorption	1.64	4.95	1.52	1.48	1.98	2.11	2.39
1D Diffusion-Reaction	2.12	13.64	1.74	1.65	2.16	2.22	2.23
1D Cahn-Hilliard	1.85	2.71	18.73	1.65	2.18	2.27	2.14
2D Shallow Water	19.11	84.40	19.81	13.77	19.23	14.55	14.01
3D Maxwell	71.15	180.53	67.56	58.28	34.95	63.21	66.33

## E. Robustness to Grid Subsampling.

We evaluate robustness to grid subsampling by testing SFO on uniformly coarsened grids. Table 9 reports performance across grid resolutions. For coarser grids (smaller  $n$ ), we enforce  $L \leq n$  by capping the number of retained modes.

Overall, subsampling generally increases the  $L_2$  relative error compared to the original-resolution setting, with the largest degradation on the higher-dimensional PDEs. However, Diffusion-Sorption contains sharp boundary-layer effects that are difficult to learn (App. F). Therefore, as the grid is coarsened (larger  $s$ ), fewer evaluation points fall in the boundary-layer region and high-frequency boundary effects are smoothed, which can reduce the measured  $L_2$  error.

Table 9.  $L_2$  relative error (%) across grid resolutions. In Diffusion-Sorption, we report  $10 \times L_2(\%)$  for readability.

<i>subsampling factor</i>	$s = 2$	$s = 4$	$s = 6$	$s = 8$	$s = 10$
1D Allen-Cahn	0.057	0.054	0.051	0.061	0.074
1D Diffusion-Sorption	1.092	1.068	0.808	0.565	0.4406
1D Diffusion-Reaction	0.236	0.292	0.288	0.282	0.360
1D Cahn-Hilliard	0.084	0.068	0.096	0.075	0.105
2D Shallow Water	0.601	0.601	0.932	1.552	1.555
3D Maxwell	38.663	43.931	49.319	58.991	62.501

For zero-shot resolution transfer, we train on a fixed spatial resolution  $n$  and evaluate on uniformly subsampled grids of size  $n/s$ . SFO keeps all learned parameters fixed and only reconstructs the Hilbert (USB) spectral basis at test time for the target resolution.

## F. Boundary Handling and Circular Convolution

SFO evaluates the USB-parameterized integral operator via FFT-based convolution, which requires a shift-invariant kernel of the form  $\kappa(x, x') = g(x - x')$  (as in FNO (Li et al., 2021) and related variants such as UNO (Rahman et al., 2023), F-FNO (Tran et al., 2023), and U-FNO (Wen et al., 2022)). On a finite discretized grid, FFT corresponds to circular convolution and thus implicitly assumes a periodic extension of the domain. This design reflects an efficiency–expressivity trade-off: FFT-based evaluation scales favorably with grid resolution, but restricts the kernel class to shift-invariant convolutions. In contrast, evaluating a general non-stationary kernel  $\kappa(x, x')$  explicitly can be more expressive (e.g., location- or input-dependent interactions), but typically incurs substantially higher computational cost (e.g., as in SVD-NO).

Table 10. Boundary vs. interior relative  $L_2$  error (in %). We report the standard full-domain relative  $L_2$  error, and additionally the error restricted to a boundary band of width  $b$  (first and last  $b$  grid points) and the remaining interior region. We set  $b = 0.1N$ . In Diffusion-Sorption, we report  $10 \times L_2(\%)$  for readability.

Dataset	Full	Boundary	Interior
1D Allen-Cahn	0.052	0.056	0.050
1D Diffusion-Sorption	1.119	1.401	0.451
1D Diffusion-Reaction	0.242	0.242	0.242
1D Cahn-Hilliard	0.072	0.081	0.069
2D Shallow Water	0.394	0.099	0.471
3D Maxwell	40.85	42.73	34.38

**Boundary vs. interior error diagnostic.** Because FFT-based evaluation corresponds to *circular* convolution, it can introduce artifacts near the domain boundaries when the underlying PDE solution is not periodic. We therefore report the standard relative  $L_2$  error on (i) the *full* spatial grid, and additionally on (ii) a *boundary band* consisting of the first and last  $b$  grid points, and (iii) the *interior* region consisting of the remaining  $N - 2b$  points. Concretely, letting  $\hat{u}, u \in \mathbb{R}^{N \times C}$  denote the predicted and ground-truth solution, we define

$$\text{Rel } L_2(\Omega)(\%) = \frac{\|\hat{u} - u\|_{2,\Omega}}{\|u\|_{2,\Omega}} \times 100,$$

where  $\Omega$  is either the full index set  $\{1, \dots, N\}$ , the boundary set  $\{1, \dots, b\} \cup \{N - b + 1, \dots, N\}$ , or the interior set  $\{b + 1, \dots, N - b\}$ . We set the band width to  $b = 0.1N$  (i.e., 10% of the grid points on each side). For multi-dimensional grids, we define the boundary band analogously as the set of points within a width- $b$  strip from the domain boundary along *any* spatial axis. Concretely, for an  $M$ -dimensional grid of size  $n^M$  (so  $N = n^M$ ), let  $b = \lfloor 0.1n \rfloor$ .

**Results.** Table 10 summarizes the results. We observe a clear separation between datasets whose solution operators are well-approximated by a *translation-invariant* kernel with *geometric decay* (as motivated in App. G) and those that are more sensitive to boundary behavior. Specifically, for Allen-Cahn, Diffusion-Reaction, and Cahn-Hilliard, the boundary and interior errors are nearly identical, consistent with the fact that these benchmarks admit a strongly shift-invariant, rapidly decaying effective kernel, for which the circular extension induced by FFT evaluation has limited impact. In contrast, Diffusion-Sorption and Maxwell exhibit a noticeable gap between boundary and interior error, indicating increased boundary sensitivity and/or less homogeneous operator behavior near the domain edges. Notably, SFO still attains lower overall error than SVD-NO on these PDEs even though SVD-NO does not impose a shift-invariance or circular-convolution constraint; this suggests that a substantial fraction of the error on this benchmark is not solely attributable to the periodic extension induced by FFT evaluation, but rather reflects intrinsic difficulty near the boundaries.

## G. Theory: Learnability of Local Stable Discretizations

We present a theoretical explanation for why Spectral Filtering Operators (SFO) can efficiently learn solution operators arising from a broad class of PDE discretizations. Our main result shows that inverse operators arising certain stable, local, shift-invariant discretizations admit approximation by SFO with logarithmic mode complexity.

For simplicity, we consider an infinite grid in which the PDE lives,  $\mathbb{Z}$ , as opposed to finite discretization. We discuss the extension to finite grids at the end of this section. For the sake of computational feasibility, we considered a centered finite window on the grid, ignoring the tails and boundary effects.

### G.1. Main theorem

**Theorem G.1** (Learnability of stable local shift-invariant discretizations). *Let  $A$  be the block three-point stencil operator on  $\ell_2(\mathbb{Z}; \mathbb{R}^d)$  defined by*

$$(Au)[i] := A_0 u[i] + A_1(u[i-1] + u[i+1]),$$

*where  $A_0, A_1 \in \mathbb{R}^{d \times d}$  are symmetric, commuting matrices. Let  $\{(a_j, b_j)\}_{j=1}^d$  denote the pairs of corresponding eigenvalues for  $A_0$  and  $A_1$ . If the stability condition  $a_j > 2|b_j|$  holds for all  $j = 1, \dots, d$ , then  $A$  is invertible and for any  $\varepsilon > 0$ , there exists an SFO-parameterized operator  $M_L$  such that*

$$\|A^{-1} - M_L\| \leq \varepsilon, \quad \text{with} \quad L = \tilde{O}(\log(1/\varepsilon)).$$

## G.2. Examples

We show certain examples where the stencil operator in G.1 naturally arises in discretization:

- Let  $u(x) \in \mathbb{R}^m$  satisfy on  $(0, 1)$  the steady coupled diffusion-reaction equation  $-Du''(x) + Ru(x) = f(x)$  with Dirichlet boundary conditions  $u(0) = u_L$ ,  $u(1) = u_R$ . Picking uniform grid  $x_0, \dots, x_{N+1}$  with  $x_i - x_{i-1} = h$ , we approximate

$$u''(x_i) = \frac{u_{i-1} - 2u_i + u_{i+1}}{h^2}$$

Plugging this into the PDE we get for  $i \in [N]$  exactly the 3 point stencil form

$$\overbrace{\left( R + \frac{2}{h^2} D \right) u_i}^{A_0} + \overbrace{\left( -\frac{1}{h^2} D \right) (u_{i-1} + u_{i+1})}^{A_1} = f_i \Rightarrow (Au)[i] = f_i$$

Stacking

$$U = (u_1, \dots, u_m), \quad F = (f_1 - B_0 u_L, f_2, \dots, f_{N-1}, f_N - A_1 u_R)$$

we can write  $AU = F$ , where  $A$  is the tridiagonal block matrix with  $A_0$  in the diagonal and  $A_1$  in the off diagonals.

- Let  $c(x, t) \in \mathbb{R}^m$  satisfy on  $(0, 1) \times (0, \infty)$  the unsteady coupled diffusion-reaction equation

$$\partial_t c(x, t) = D c''(x, t) - R c(x, t) + s(x),$$

with Dirichlet boundary conditions  $c(0, t) = u_L$ ,  $c(1, t) = u_R$  and initial condition  $c(x, 0) = c_0(x)$ . Picking the same uniform grid  $x_0, \dots, x_{N+1}$  with spacing  $h$ , we approximate for  $i \in [N]$

$$c''(x_i, t) \approx \frac{c_{i-1}(t) - 2c_i(t) + c_{i+1}(t)}{h^2}.$$

Plugging into the PDE gives the semi-discrete (method-of-lines) system

$$\dot{c}_i(t) = \frac{1}{h^2} D (c_{i-1}(t) - 2c_i(t) + c_{i+1}(t)) - R c_i(t) + s_i.$$

Rearranging yields the same 3-point stencil operator acting on the spatial grid function:

$$\overbrace{\left( R + \frac{2}{h^2} D \right) c_i(t)}^{A_0} + \overbrace{\left( -\frac{1}{h^2} D \right) (c_{i-1}(t) + c_{i+1}(t))}^{A_1} = s_i - \dot{c}_i(t) \Rightarrow (Gc(t))[i] = s_i - \dot{c}_i(t),$$

where  $(Gc)[i] = A_0 c_i + A_1 (c_{i-1} + c_{i+1})$ . Stacking interior unknowns

$$C(t) = (c_1(t), \dots, c_N(t)), \quad S = (s_1 - A_1 u_L, s_2, \dots, s_{N-1}, s_N - A_1 u_R),$$

we obtain  $\dot{C}(t) = -G C(t) + S$  where  $G$  is as before.

## G.3. Proof idea

The proof decomposes into two conceptual steps.

**Step 1: Locality and stability imply exponential decay.** It is a classical result in numerical analysis and operator theory that the inverse of a banded, well-conditioned operator exhibits exponential off-diagonal decay (see, e.g., (Demko et al., 1984; Benzi, 2007)). In our setting, this implies that the inverse of a stable local stencil operator has a Green's function that decays exponentially with spatial distance. We include a short proof in the simplest stencil case for completeness.

**Step 2: Exponential decay implies spectral filter learnability.** Results from the spectral filtering literature show that exponentially decaying impulse responses admit accurate approximation using a small number of Hankel/USB modes. In particular, the projection error onto the top spectral filtering modes decays exponentially, yielding logarithmic mode complexity (Hazan et al., 2017).

#### G.4. Setup and Notation

Let  $M : (\mathbb{R}^d)^\mathbb{Z} \rightarrow (\mathbb{R}^d)^\mathbb{Z}$  be an operator on vector fields on the infinite discrete grid  $\mathbb{Z}$ , and let  $u : \mathbb{Z} \rightarrow \mathbb{R}^d$ . We say that  $M$  is *translation-equivariant* if

$$\tau_s M(u) = M(\tau_s u) \quad \text{for all } s \in \mathbb{Z},$$

where  $\tau_s$  is the right-shift operator  $(\tau_s u)[i] = u[i - s]$ . It can be seen that the 3-point stencil operator  $A$  in G.1 is linear and translation-equivariant.

Assume in addition that  $M$  is invertible (as an operator on a suitable sequence space so that the convolutions below are well-defined). Define the matrix-valued impulse response (Green's kernel) of  $M$  by

$$G := M^{-1} \delta_0 \text{Id} \in (\mathbb{R}^{d \times d})^\mathbb{Z}.$$

where  $\delta_0[i] = \mathbf{1}_{(i=0)}$  is the Dirac distribution. Equivalently,  $G$  satisfies

$$M(G) = \delta_0 \text{Id}.$$

Then, for any  $v$  for which the series converges,  $M^{-1}$  acts by discrete convolution with  $G$ :

$$(M^{-1}v)[i] = (G * v)[i] := \sum_{j \in \mathbb{Z}} G[i - j] v[j]. \quad (15)$$

We call  $G$  the *Green's kernel* of  $M$ . This terminology mirrors PDE theory: the Green's function  $G(x, s)$  of a linear PDE  $\mathcal{L}u = f$  satisfies

$$\mathcal{L}u = f \Rightarrow u(x) = (\mathcal{L}^{-1}f)(x) = \int G(x, s) f(s) ds. \quad (16)$$

If  $\mathcal{L}$  (and its discretization) is translation-invariant, then  $G(x, s) = G(x - s)$ , and (16) reduces to a convolution representation, matching (15). In this setting,  $M$  discretizes  $\mathcal{L}$ , and  $M^{-1}$  is the discrete solution operator.

#### G.5. Lemma 1: Local stability implies exponential decay

**Lemma G.2** (Block stencil yields matrix-valued exponential decay). *Under the assumptions of Theorem G.1,  $A$  is linear, translation-equivariant, and invertible, and its Green's function  $G$  can be written as a symmetric, matrix-valued exponentially decaying function:*

$$G[t] = \sum_{k=1}^d \Theta_k r_k^{|t|}, \quad |r_k| < 1$$

*Proof.* Since  $A_0, B_0 \in \mathbb{R}^{d \times d}$  are symmetric and commute, they are simultaneously orthogonally diagonalizable: there exists an orthogonal matrix  $U$  such that

$$A_0 = U \text{diag}(\alpha_1, \dots, \alpha_d) U^\top, \quad B_0 = U \text{diag}(\beta_1, \dots, \beta_d) U^\top,$$

Writing  $\tilde{u} := U^\top u$  and  $\tilde{v} := U^\top v$ , the equation  $Au = v$  decouples into

$$\alpha_k \tilde{u}_k[t] + \beta_k (\tilde{u}_k[t-1] + \tilde{u}_k[t+1]) = \tilde{v}_k[t], \quad k = 1, \dots, d.$$

Equivalently, for each  $k$  define the scalar operator on  $\ell^2(\mathbb{Z})$

$$(\tilde{A}^{(k)} w)[t] := \beta_k w[t-1] + \alpha_k w[t] + \beta_k w[t+1].$$

Let  $S : \ell^2(\mathbb{Z}) \rightarrow \ell^2(\mathbb{Z})$  be the shift  $(Sw)[t] = w[t-1]$ , so  $S$  is unitary and  $\|S\| = \|S^{-1}\| = 1$ . Then

$$\tilde{A}^{(k)} = \alpha_k \left( I + \frac{\beta_k}{\alpha_k} (S + S^{-1}) \right), \quad \left\| \frac{\beta_k}{\alpha_k} (S + S^{-1}) \right\| \leq \frac{2|\beta_k|}{\alpha_k} < 1.$$

Hence  $I + \frac{\beta_k}{\alpha_k} (S + S^{-1})$  is invertible by the Neumann series, so each  $\tilde{A}^{(k)}$  is invertible on  $\ell^2(\mathbb{Z})$ , and therefore  $A$  is invertible on  $\ell^2(\mathbb{Z}; \mathbb{R}^d)$ .

Since  $A$  has constant coefficients, it commutes with lattice shifts  $(T_s u)[t] = u[t - s]$ , i.e. it is translation equivariant. Since  $A$  is linear, translation equivariant, and invertible, it admits a Green's kernel  $G : \mathbb{Z} \rightarrow \mathbb{R}^{d \times d}$ .

In the  $U$ -basis,

$$\tilde{G}[t] := U^\top G[t] U = \text{diag}(g_1[t], \dots, g_d[t]),$$

and each  $g_k$  satisfies

$$\beta_k g_k[t - 1] + \alpha_k g_k[t] + \beta_k g_k[t + 1] = \mathbf{1}_{(t=0)}.$$

If  $\beta_k = 0$ , then  $g_k[t] = \mathbf{1}_{(t=0)} / \alpha_k$ . Assume  $\beta_k \neq 0$ . For  $t \neq 0$  we have the homogeneous recurrence with characteristic equation

$$\beta_k r^2 + \alpha_k r + \beta_k = 0,$$

with distinct real roots  $r_k^\pm$  satisfying  $r_k^+ r_k^- = 1$ . Let  $r_k$  be the root with  $|r_k| < 1$ , i.e.

$$r_k = \frac{-\alpha_k + \sqrt{\alpha_k^2 - 4\beta_k^2}}{2\beta_k}, \quad |r_k| < 1.$$

$\ell^2$ -decay forces  $g_k[t] = c_+ r_k^t$  for  $t > 0$  and  $g_k[t] = c_- r_k^{-t}$  for  $t < 0$ . Since both the operator and the forcing  $\delta_0$  are invariant under reflection  $t \mapsto -t$ , if  $g_k$  solves the impulse equation then so does  $t \mapsto g_k[-t]$ ; by uniqueness (invertibility of  $\tilde{A}^{(k)}$ ) we have  $g_k[t] = g_k[-t]$ , hence  $c_+ = c_- =: C_k$  and

$$g_k[t] = C_k r_k^{|t|}.$$

Imposing the equation at  $t = 0$  gives

$$\beta_k g_k[-1] + \alpha_k g_k[0] + \beta_k g_k[1] = 1 \implies C_k(\alpha_k + 2\beta_k r_k) = 1.$$

With the above choice of  $r_k$ ,  $\alpha_k + 2\beta_k r_k = \sqrt{\alpha_k^2 - 4\beta_k^2}$ , hence

$$g_k[t] = \frac{r_k^{|t|}}{\sqrt{\alpha_k^2 - 4\beta_k^2}} \quad (\beta_k \neq 0).$$

Finally, we obtain

$$G[t] = U \text{ diag}(g_1[t], \dots, g_d[t]) U^\top = \sum_{k=1}^d \Theta_k r_k^{|t|}, \quad \Theta_k := \frac{1}{\sqrt{\alpha_k^2 - 4\beta_k^2}} U_{\cdot, k} U_{\cdot, k}^\top,$$

□

#### G.6. Lemma 2: Exponential decay implies spectral filter learnability

**Lemma G.3** (Spectral filtering approximation for exponentially decaying kernels (Hazan et al., 2017, Lem. 4.1)). *Let  $G : \mathbb{Z} \rightarrow \mathbb{R}^{d \times d}$  satisfy  $G[t] = \sum_{k=1}^d \Theta_k r_k^{|t|}$  for  $|r_k| < 1$ . Pick  $N \geq 1$ , and restrict  $G$  to  $\{0, 1, \dots, N\}$ . Then for every  $\varepsilon > 0$ , there exists a kernel  $g_L$  in the span of the first  $L$  Hankel/USB spectral filtering modes such that*

$$\|g - g_L\|_{\ell_2} \leq \varepsilon,$$

with

$$L = \tilde{O}(\log(1/\varepsilon)).$$

*Proof sketch.* Exponentially decaying finite sequences are impulse responses of finite-horizon stable linear dynamical systems. The spectral filtering framework of (Hazan et al., 2017) shows that such responses admit exponentially accurate approximation by projection onto the top eigenvectors of an associated Hankel matrix, with error controlled by the tail of its spectrum (Lemma 4.1 therein). Moreover, the Hankel spectrum decays exponentially (see Chapter 11 of (Hazan & Singh, 2022)), yielding the stated logarithmic mode complexity.

*Remark:* The spectral filtering framework is defined for finite-horizon LDS. However,  $G$  is defined on the infinite grid  $\mathbb{Z}$  and is symmetric around 0. Therefore only approximate  $G[0 : N]$  with truncation error controlled by  $N$  due to the exponentially decaying tails of  $G$ . □

We can now prove Theorem G.1 as a simple consequence of the proceeding two lemmas:

*Proof of Theorem G.1.* By Lemma G.2, the inverse operator  $A^{-1}$  has an exponentially decaying Green's function. Lemma G.3 therefore yields an SFO-parameterized operator  $M_L$  approximating  $A^{-1}$  to accuracy  $\varepsilon$  using  $L = \tilde{O}(\log(1/\varepsilon))$  modes.  $\square$

**Remark (Generalization to General Stable Stencils)** The exponential decay property holds for any stable, local, shift-invariant discretization, not just the three-point stencil. This fact is known in the literature (Benzi, 2007). By itself, exponential decay does not immediately imply learnability by spectral filtering. However, the exponential decay arising in these cases may be developed into a linear dynamical structure, as we did for the three point stencil, which is then learnable by spectral filtering.

**Remark (Marginal Stability and Long-Range Dependencies).** A key advantage of the spectral filtering framework is its robustness to *marginal stability* ( $|\rho| \rightarrow 1$ ). In this regime, the Green's function decays slowly (e.g., polynomially), corresponding to long-range spatial dependencies common in transport-dominated PDEs (e.g., Shallow Water, Maxwell). Unlike local basis expansions which struggle to capture such non-local interactions efficiently, the Hankel/USB modes remain highly effective for polynomially decaying kernels, ensuring that SFO performs well even when the system operates near the stability boundary (Hazan et al., 2017).